

Ghost Artifact Reduction for Echo Planar Imaging Using Image Phase Correction

Michael H. Buonocore, Lisheng Gao

An algorithm is described for reducing ghost artifacts in echo planar imaging (EPI) using phase corrections derived from images reconstructed using only even or odd k -space lines. The $N/2$ ghost, that arises principally from time-reversal of alternate k -space lines, was significantly reduced by this algorithm without the need for a calibration scan. In images obtained in eight subjects undergoing EPI for auditory functional MRI (fMRI) experiments, $N/2$ ghost intensity was reduced from $10.3\% \pm 2.1\%$ (range: 7.9–14.1%) to $4.5\% \pm 0.2\%$ (range: 4.1–4.9%) of parent image intensity, corresponding to a percent reduction in ghost intensity of $54\% \pm 9\%$ (range: 43–65%), and the algorithm restored this intensity to the parent image. It provided a significant improvement in image appearance, and increased the correlation coefficients related to neural activation in functional MRI studies. The algorithm provided reduction of artifacts from all polynomial orders of spatial phase errors in both spatial directions. The algorithm did not eliminate $N/2$ ghost intensity contributed by field inhomogeneities, susceptibility, or chemical shift.

Key words: magnetic resonance imaging; echo planar imaging; image processing; artifacts.

INTRODUCTION

It is not uncommon for the raw data on each line of k -space to be offset relative to the true center of k -space due to spin physical effects, imperfect gradient action, and data acquisition system performance (1–3). This does not cause a problem in standard reconstruction because each line of k -space is traversed in the same direction and all k -space lines have nearly the same offset. This leads to a constant phase factor in the reconstructed image that does not appear in the magnitude image. However, in echo-planar imaging, alternate k -space lines are traversed in opposite directions. Before standard Fourier reconstruction, either odd or even lines must be time-reversed to place the data points at their correct location in k -space. This reversal results in alternating offset of the lines, which in the spatial domain results in signal intensity displaced halfway across the image in the phase encode direction. Given N pixels across the FOV, this “ghost image” or simply “ghost,” is shifted $N/2$ pixels relative to the “parent image” positioned at the correct location.

MRM 38:89–100 (1997)

From the Department of Radiology, UC Davis Medical Center, Sacramento, California (M.H.B.) and KLA Instruments Corp., San Jose, California (L.G.). Address correspondence to: Michael H. Buonocore, M.D., Ph.D., Department of Radiology, TICON-II, 2nd floor, UC Davis Medical Center, Sacramento, CA 95817.

Received January 25, 1996; revised September 20, 1996; accepted January 8, 1997

This work was presented at the RSNA 80th Scientific Assembly and Annual Meeting, Nov. 27–Dec. 2, 1994, Chicago.

0740-3194/97 \$3.00

Copyright © 1997 by Williams & Wilkins

All rights of reproduction in any form reserved.

A significant source of these echo offsets is eddy currents (4). The magnetic fields induced by eddy currents effectively delay or advance the time of refocussing of the spins as a function of spatial position, so that when the zeroth moment of the gradient waveform is zero, there remains a spatially dependent residual phase at each pixel across the object. Time-domain filters are routinely employed to create a compensated waveform that produces a perfect trapezoid gradient response in the presence of eddy currents, but the spatially dependent eddy current effects cannot be eliminated entirely. Echo offsets also result from off-resonance phase errors caused by field inhomogeneity, susceptibility, and chemical shift (5, 6). In this paper, these sources are collectively referred to as main field distortions. Spin phases evolve smoothly under these distortions during the echo train and correspond to single frequencies in k -space. However, time-reversal of alternating lines of k -space creates a strong discontinuity of the phase that maps to multiple frequencies in k -space. To reduce this effect, special pulse sequencing is required in multishot EPI and related sequences (5). Another source of offset is analog low pass filtering of the raw data which generates, due to causality, a slightly asymmetrical location of the echo (3, 7).

The most successful ghost reduction method to date uses a so-called calibration scan acquired with the phase encode (y) gradient off (3, 8–10). The calibration scan determines the offset of the echo center for each k_y line of k -space. Significant relative offsets of the odd and even echos are typically observed in this scan. However, because the time of the echo peak is inherently sensitive to main field distortions, only an average offset between even and odd lines is reliably determined (8). The even or odd line having the highest intensity data point is used to determine the offset for all the similar (i.e., even or odd) lines. The next line is used to determine the offset for the other (i.e., odd or even) lines. The temporal offsets are set to the nearest sampling point by this analysis. Subsample offsets are extracted from the observed linear phase shifts in the frequency encode (x) direction in the (x, k_y) domain. The raw data is also corrected with respect to constant phase differences between odd and even lines using projection of the phase along k_y in the (x, k_y) domain. The calibration scan can be easily incorporated into the beginning of the imaging sequence to retain the “snap-shot” capability of EPI (9). It is unlikely that these extra acquisitions would adversely affect any experimental design. In principal, the calibration scan correction simultaneously removes linear and zeroth order phase errors and significantly decreases the ghost intensity. However, in practice, it can occasionally increase the $N/2$ ghost. The echo center may be different from the echo center in the data due to variations in system behavior and patient motion, the echo peak may

be clipped by the A/D converter, or higher order phase errors may be significant.

For these reasons, we investigated phase correction algorithms that would not require a calibration scan. Reduction of ghost artifact by 2D filtering of images derived from separated even and odd echos was first described by Bruder in his paper on image reconstruction for EPI using nonequidistant k -space sampling (3). The algorithm outlined in that paper (3, pp. 320–321) is a special case of the algorithm described here in which correctable spatial phase errors are derivable from point spread functions of k_x convolved with the raw data. Our algorithm corrects not only constant echo offset, which corresponds to linear phase errors in the spatial domain along x , but also zero and higher order phase errors in both x and y corresponding to more complicated eddy current effects.

METHODS

Signal and Image Model

The reconstructed image can be decomposed into a sum of two complex images, one reconstructed from the odd lines of k -space and another from the even lines. The raw data is given by

$$S(t, k_y) = \iint M(x, y) \exp(i\theta(x, y)) \exp(-i\gamma G_x t x) \exp(-ik_y y) dx dy \quad [1]$$

for $k_y = n\Delta k_y$, n even, $-N/2 \leq n \leq N/2 - 1$, and

$$S(t, k_y) = \iint M(x, y) \exp(-i\theta(x, y)) \exp(+i\gamma G_x t x) \exp(-ik_y y) dx dy \quad [2]$$

for $k_y = n\Delta k_y$, n odd, $-N/2 \leq n \leq N/2 - 1$. Here, $M(x, y)$ is the object being reconstructed, k_y is the phase encode spatial frequency, Δk_y is the phase encode spatial frequency increment, G_x is the strength of the frequency encode gradient, t is a time point of data acquisition, and $\theta(x, y)$ represents phase errors at the echo center due to gradient dependent main field offsets, echo delays, and echo drifts. Boesch *et al.* (4) characterized not only time-dependent phase errors having linear spatial dependence, but also those with higher order as well as no spatial dependence. Eddy current phase errors can be represented by the model provided that they have the property of polarity reversal upon reversal of the polarity of the causative gradient. This is a reasonable physical assumption for eddy currents. Main field offset and constant echo delay are represented by $\theta(x, y) = \theta_0 + x\theta_1$. Here, θ_0, θ_1 are constants with $\theta_1 = \gamma G_x s$, where s is the physical time delay of the echo as would be observed in a calibration scan. The equations assume that even and odd echos are effected by the same phase accumulations, but in opposite directions. To fill k -space correctly (i.e., all lines of k -space have the same $\exp(-i\gamma t)$ factor), $S(t, k_y)$ for k_y odd must be time reversed. That is, $t \rightarrow -t$ in Eq. [2] above.

With the specification that the object is defined at $N \times N$ integer-valued points (x, y) in the spatial domain,

the conjugate spatial and frequency variables can be regarded as dimensionless, and the signal S at points labeled by integers (n, m) in k -space can be written

$$S(m, n) = \begin{cases} \sum_x \sum_y M(x, y) \exp(i\theta(x, y)) \exp\left(-i \frac{2\pi}{N} mx\right) \exp\left(-i \frac{2\pi}{N} ny\right) & \text{for } n \text{ even} \\ \sum_x \sum_y M(x, y) \exp(-i\theta(x, y)) \exp\left(-i \frac{2\pi}{N} mx\right) \exp\left(-i \frac{2\pi}{N} ny\right) & \text{for } n \text{ odd} \end{cases} \quad [3]$$

where $k_x = 2\pi m/N$, $k_y = 2\pi n/N$, $-N/2 \leq m \leq N/2 - 1$, and $-N/2 \leq n \leq N/2 - 1$. Spatial coordinates are expressed in pixels, and spatial frequency in radians per pixel. The calibration scan estimates $\theta(x, y) = \theta_0 + x\theta_1$ directly from the echo train data. Image phase correction estimates general $\theta(x, y)$ by evaluating images reconstructed separately from the odd and even lines of k -space. Image phase correction is derived by first applying the discrete inverse Fourier transform (IFT) to S to produce the reconstructed image $\hat{M}(x, y)$ given by

$$\hat{M}(x, y) = (1/N^2) \sum_m \sum_n S(m, n) \exp\left(i \frac{2\pi}{N} mx\right) \exp\left(i \frac{2\pi}{N} ny\right) \quad [4]$$

Using Eq. [3] with

$$\sum_{m \text{ even}} \dots = \sum_m \frac{1}{2} (1 + \exp(i\pi m)) \dots = \sum_m \frac{1}{2} \left(1 + \exp\left(i \frac{2\pi}{N} m \left(\frac{N}{2}\right)\right)\right) \dots \quad [5]$$

and

$$\sum_{m \text{ odd}} \dots = \sum_m \frac{1}{2} (1 - \exp(i\pi m)) \dots = \sum_m \frac{1}{2} \left(1 - \exp\left(i \frac{2\pi}{N} m \left(\frac{N}{2}\right)\right)\right) \dots \quad [6]$$

Eq. [4] can be rewritten

$$\hat{M}(x, y) = \hat{M}_{\text{even}}(x, y) + \hat{M}_{\text{odd}}(x, y) \quad [7]$$

where

$$\begin{aligned} \hat{M}_{\text{even}}(x, y) &\equiv \frac{1}{2} \left(M(x, y) \exp(i\theta(x, y)) \right. \\ &\quad \left. + M\left(x, y - \frac{N}{2}\right) \exp\left(i\theta\left(x, y - \frac{N}{2}\right)\right) \right) \\ \hat{M}_{\text{odd}}(x, y) &\equiv \frac{1}{2} \left(M(x, y) \exp(-i\theta(x, y)) \right. \\ &\quad \left. - M\left(x, y - \frac{N}{2}\right) \exp\left(-i\theta\left(x, y - \frac{N}{2}\right)\right) \right) \end{aligned} \quad [8]$$

or, equivalently,

$$\hat{M}(x, y) = \hat{M}_{\text{parent}}(x, y) + \hat{M}_{\text{ghost}}(x, y) \quad [9]$$

where

$$\begin{aligned} \hat{M}_{\text{parent}}(x, y) &\equiv M(x, y)\cos(\theta(x, y)) \\ \hat{M}_{\text{ghost}}(x, y) &\equiv i M\left(x, y - \frac{N}{2}\right) \\ &\quad \sin\left(\theta\left(x, y - \frac{N}{2}\right)\right) \end{aligned} \quad [10]$$

Referring to Eq. [7], \hat{M}_{even} is reconstructed using only the even k -space lines, and \hat{M}_{odd} is reconstructed using only the odd lines, with zero filling of missing lines. In Eq. [9], $\hat{M}_{\text{parent}}(x, y)$ is positioned correctly, and $\hat{M}_{\text{ghost}}(x, y)$ is shifted by $N/2$ pixels relative to the parent image.

Correcting the Phase

Phase errors can be extracted only from pixels in non-overlapping regions of the parent image and ghost. The user first draws a large region of interest (ROI) within or precisely enclosing the parent image. The “parent-only” region is then defined (by the computer program) as the collection of pixels (x, y) within this ROI having $N/2$ shifted pixels $(x, y - N/2)$ that lie *outside* this ROI. A threshold is applied to reject pixels within the ROI whose amplitudes are near background noise level. Within the parent-only region, $M(x, y - N/2) = 0$, and Eq. [8] shows that the difference in the phase angles between \hat{M}_{odd} and \hat{M}_{even} is $2\theta(x, y)$. In the ghost-only region, the difference in the phase angles between \hat{M}_{odd} and \hat{M}_{even} is $\pi + 2\theta(x, y - N/2)$, where π arises from the -1 multiplying $M(x, y - N/2)$ in \hat{M}_{odd} . Outside the object in the frequency direction, the difference in the phase angles can be estimated by linear extrapolation.

To eliminate $\hat{M}_{\text{ghost}}(x, y)$, data is modified such that the phase differences between \hat{M}_{even} and \hat{M}_{odd} are near zero in the parent-only region. There are different points in the reconstruction process in which the correction is easiest to apply depending on whether $\theta \approx x$, $\theta = \theta(x)$, or $\theta = \theta(x, y)$ is used. The most direct algorithm, which can be used if parent image and ghost do not overlap, derives from Eq. [9] and [10]. $\hat{M}_{\text{parent}}(x, y)$ can be combined pixel-by-pixel with $\hat{M}_{\text{ghost}}(x, y - N/2)$ to give the corrected image $\hat{M}_c(x, y)$,

$$\begin{aligned} \hat{M}_c(x, y) &= \hat{M}_{\text{parent}}(x, y)\cos(\theta(x, y)) \\ &\quad - i\hat{M}_{\text{ghost}}\left(x, y - \frac{N}{2}\right)\sin(\theta(x, y)) \end{aligned} \quad [11]$$

which is equal to $M(x, y)$. Equivalently, even and odd images can be multiplied by $\exp(-i\theta(x, y))$ and $\exp(i\theta(x, y))$, respectively, and combined to give

$$\begin{aligned} \hat{M}_c(x, y) &= \hat{M}_{\text{even}}(x, y)\exp(-i\theta(x, y)) \\ &\quad + \hat{M}_{\text{odd}}(x, y)\exp(i\theta(x, y)) \end{aligned} \quad [12]$$

which is equal to $M(x, y)$ in the parent-only region. When there is overlap, $\theta(x, y)$ within the parent-only region can be averaged over y and is typically best fit to a linear

function of x , or left as a general function of x . When $\theta \approx x$, the correction is equivalent to a single constant phase offset θ_0 and time offset s that can be applied directly to the raw data, as is done when using the calibration scan (8). When $\theta = \theta(x)$, the phase correction is typically applied before the k_y IFT, when the data is in the (x, k_y) domain. After substitution of Eq. [3], and carrying out the k_x IFT, Eq. [4] can be written

$$\hat{M}(x, y) = (1/N) \sum_n \tilde{M}(x, n)\exp\left(i\frac{2\pi}{N}ny\right) \quad [13]$$

where

$$\tilde{M}(x, n) \equiv \begin{cases} \sum_{y'} M(x, y')\exp(i\theta(x)) \\ \exp\left(-i\frac{2\pi}{N}ny'\right) & n \text{ even} \\ \sum_{y'} M(x, y')\exp(-i\theta(x)) \\ \exp\left(-i\frac{2\pi}{N}ny'\right) & n \text{ odd} \end{cases} \quad [14]$$

represents the partially processed raw data in the (x, k_y) domain. In this domain, multiplicative factors $\exp(-i\theta(x))$ and $\exp(i\theta(x))$ can be applied to even and odd k -space lines, respectively, prior to k_y IFT (i.e., summation over n), leading to corrected data

$$\tilde{M}_c(x, n) \equiv \sum_{y'} M(x, y')\exp\left(-i\frac{2\pi}{N}ny'\right) \quad \text{all } n \quad [15]$$

and corrected image

$$\hat{M}_c(x, y) = (1/N) \sum_n \tilde{M}_c(x, n)\exp\left(i\frac{2\pi}{N}ny\right) \quad [16]$$

which is equal to $M(x, y)$. The algorithm using $\theta = \theta(x)$ is demonstrated with simulated raw data from a uniform ellipse (Fig. 1), and with real raw data from an axial brain scan (Fig. 2). In these examples, the effect of phase correction on raw data, partially processed data in the (x, k_y) domain, and the image can be easily evaluated and compared against the equations.

Algorithm Evaluation

Because field of view is typically set to the margins of the object, parent image and ghost overlap significantly. Therefore the algorithm was tested using $\theta = \theta(x)$. Algorithm evaluation was done using images from eight auditory fMRI studies (carried out between May 25, 1994 and Jan 25, 1995) designed to measure the cerebral cortical response to spoken words in normal subjects (11). All subjects gave informed consent. The scans were performed using a local gradient coil (Medical Advances, Inc., Milwaukee, WI) that attaches to the standard Signa 1.5T MR imaging system (GE Medical Systems, Waukesha, WI). T_2^* -weighted echo planar imaging (EPI) was used with the following parameters: gradient recalled echo, coronal plane, TR : 2000 ms, effective TE : 40 ms, flip angle: 90 degrees, matrix: 64×64 , FOV: 22 cm, slice:

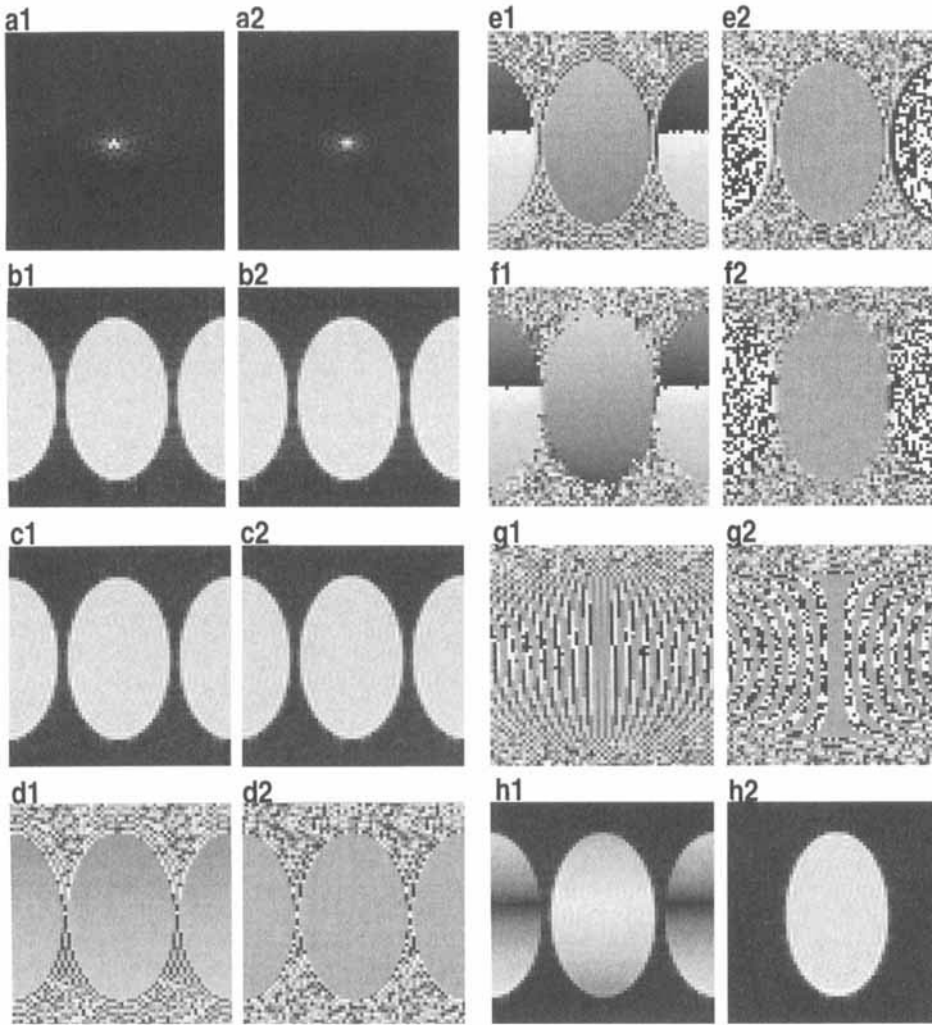


FIG. 1. Computer simulation of EPI raw data acquisition and image phase correction. Signal from ellipse (8.5 cm major axis, 5.5 cm minor axis, FOV = 20, Matrix = 64) is computed analytically (24) and image phase correction applied using $\theta(x)$ model, Eqs. [13] through [16]. EPI data acquisition is taken using $\theta_0 = \pi/20$ and $\theta_1 = -\pi(x/64)$ to generate $N/2$ ghost artifact based on Eq. [3], where θ_0 and θ_1 correspond to the zeroth and linear terms of $\theta(x)$. These numbers were chosen to mimic the ghost artifact seen in the axial EPI scans in Fig. 2. Peak-to-peak random noise, equal to 1/16 of the root mean square image intensity, was added to the raw data. Time reversal of odd k_y lines was applied prior to display. Images are organized in two double-columns, with original (those having no correction) labeled "1" and corrected (those having image phase correction) labeled "2" on left and right of each double-column, respectively. In all pictures, x (frequency encode) direction is vertical (increasing downward), and y (phase encode) direction is horizontal. Amplitude is positive (0: dark, maximum amplitude: bright), and phase is in range $-\pi$ (dark) to π (bright). (a) Amplitude of raw data (Eq. [3]). The θ_0 reflects a 1/2 pixel temporal shift s_0 of the raw data (s_0 is negative, corresponding to temporal advance of peak amplitude at $k_y = 0$), of even and odd lines in

opposite directions. Corrected raw data is computed by IFT of data corrected in (x, k_y) space (Eq. [15]). (b) Amplitude image reconstructed obtained from even k -space lines, with odd k -space lines set to zero (Eq. [8]). Original and corrected (Eq. [16]) amplitude images are identical. (c) Amplitude image reconstructed from odd k -space lines, with even k -space lines set to zero (Eq. [8]). Original and corrected (Eq. [16]) amplitude images are identical. (d) Phase of image reconstructed from even k -space lines, revealing $\theta(x, y)$ (Eq. [8]). Original shows smooth phase variation along x -direction, $-\pi/2$ (top) to $\pi/2$ (bottom). Corrected image (Eq. [16]) has no such variation. (e) Phase image from odd k -space lines revealing same $\theta(x, y)$ and relative π shift of ghost phase (Eq. [8]). Original shows smooth phase variation across x -direction, $+\pi/2$ (top) to $-\pi/2$ (bottom), opposite to that in (d). In the ghost, the phase is offset by π , but the trend is the same as in the parent image (Eq. [8]). The black/white transition occurs at the incremental transition from π to $-\pi$. Corrected image (Eq. [16]) shows no smooth phase variation. The phase of the ghost is speckled black and white in the corrected image due to small random angle variations (± 2 degrees) around the black/white transition at $-\pi$. (f) Difference between phase images obtained from even and odd k -space lines (Eq. [8]). In the parent image, the phase difference varies from π (top) to $-\pi$ (bottom), essentially twice as much variation as in even and odd phase images alone. The ghost image shows the π offset, with the same trend and range. Corrected image (Eq. [16]) shows no phase shift. The phase of the ghost is speckled (black and white) in the corrected image, a result of small random angle variations (± 2 degrees) around the black/white transition at $-\pi$. (g) Phase images of data in (x, k_y) space (obtained by 1D-FT of raw data in x direction). Original (x, k_y) phase data shows vertical lines at even k_y values with increasing linear phase from top to bottom alternating with odd k_y lines showing decreasing linear phase from top to bottom (phase terms in Eq. [14]). Linear phase from top to bottom is eliminated in the corrected (x, k_y) data, leaving (x, k_y) phase distribution consistent with ellipse (Eq. [15]). (h) In original amplitude image, amplitude variations are consistent with first order phase errors $\theta(x, y) = \theta_0 + x\theta_1$, (Eq. [10]). Ghost and amplitude variations are eliminated by correction (Eq. [15]).

6 mm, gap: 2 mm, range (typical): -80 mm to $+40$ mm by Talairach and Tournoux (12) AP coordinates, slice locations: 16, images at each slice location (repetitions): 144, scan time: 4 min 48 s, fat saturation on. Digital audio files were played through an MR compatible audio system (Resonance Technology, Inc., Van Nuys, CA). In the scan used for algorithm evaluation, baseline images were ac-

quired for 32 s with no auditory stimuli, followed by eight 32-s cycles during which, in each cycle, common words were presented at 0.5 Hz for 16 s, followed by no words for 16 s. Neural activation by this method was strong and largely limited to temporal gyri bilaterally in all studies. Images were reconstructed from the raw data using no phase correction and using image phase

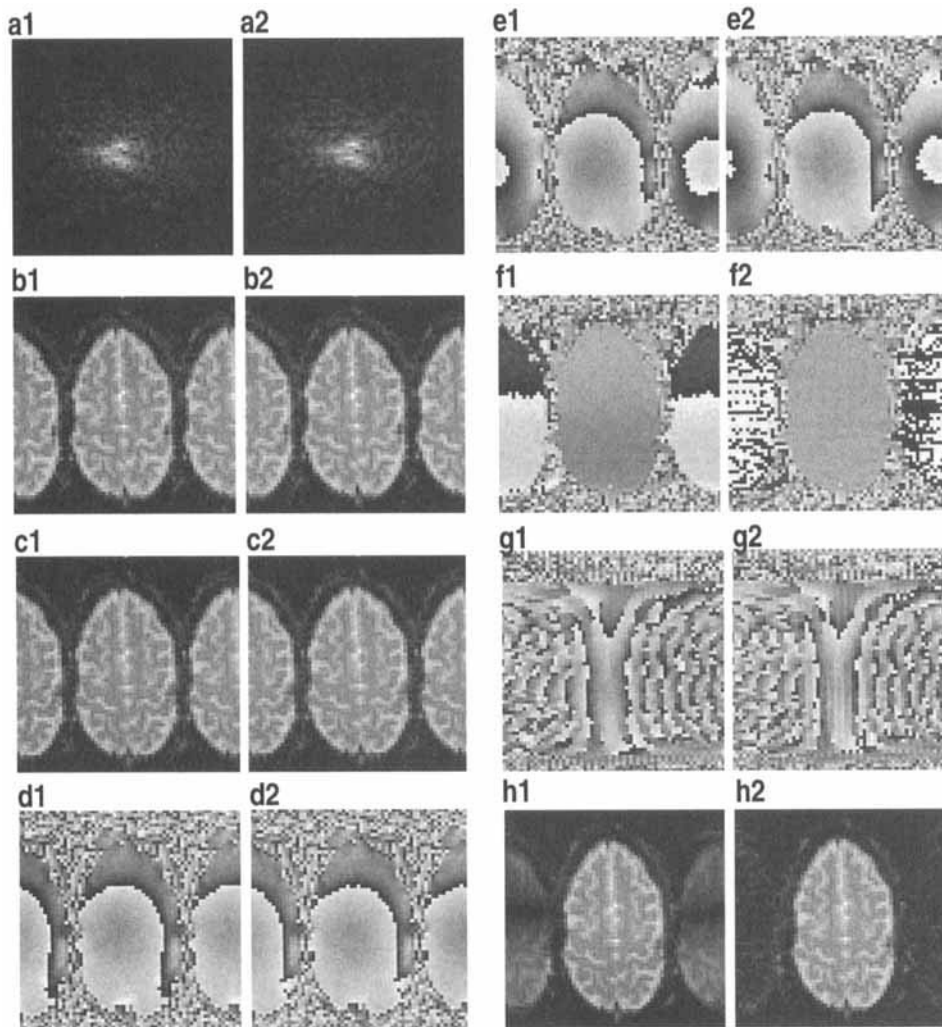


FIG. 2. Axial EPI head scan showing $N/2$ ghost artifact and image phase correction. Correction using $\theta(x)$ model, Eqs. [13] through [16]. Images are organized as in Fig. 1. Time reversal of odd k_y lines applied prior to display. (a) Amplitude of raw data. A time delay corresponding to θ_1 of about $-2\pi/3(x/64)$ is seen as a slight (<1 pixel) broadening of original raw data relative to corrected raw data. (b) Amplitude image obtained from even k -space lines (odd k -space lines set to zero). Original and corrected amplitude images are identical. (c) Amplitude image from odd k -space lines (even k -space lines set to zero). Original and corrected amplitude images are identical. (d) Phase image from even k -space lines. Original shows smooth phase variation along x direction, approximately $-\pi/6$ (top) to $\pi/6$ (bottom), superimposed on a complicated phase structure. The same smooth phase variation occurs in parent image and ghost. Image phase corrected image has no such variation. (e) Phase image from odd k -space lines. Original shows smooth phase variation across x direction, $+\pi/6$ (top) to $-\pi/6$ (bottom), opposite to that in (d), superimposed on a complicated phase structure similar to that obtained with even k -space lines. In the ghost, the phase is offset by π , but the smooth variation is the same as in the parent image. The black/white transition occurs at

the incremental transition from π to $-\pi$. Corrected image shows no such variation. (f) Difference between odd and even phase images. The complicated phase structure is eliminated, revealing clearly the phase shifts eliminated with phase correction. In the parent image, the phase difference smoothly varies from about $\pi/3$ (top) to $-\pi/3$ (bottom). The ghost image shows the same trend and range of phases, offset by π . The black/white transition in the ghost occurs at the incremental transition from $-\pi$ to π . Corrected image shows no phase shift. The phase of the ghost is speckled black and white in the corrected image, a result of small random angle variations (± 2 degrees) around the black/white transition at $-\pi$. Note the similarity of these images to those obtained with computer simulation of EPI acquisition in Fig. 1. $\theta(x,y)$ is predominantly independent of y except at points having obvious second sources of phase, e.g., sagittal sinus having venous flow. (g) Phase images of data in (x,k_y) space (obtained by 1DFT of raw data in x direction). Original (x,k_y) data shows vertical lines at even k_y values with increasing linear phase from top to bottom (i.e., along x) alternating with odd k_y lines showing decreasing linear phase from top to bottom. Linear phase from top to bottom is eliminated in the corrected (x,k_y) data (leaving phase structure consistent with the actual ellipse). (h) Amplitude of reconstructed images. In original, there are amplitude variations consistent with Eq. [10], using $\theta_0 = -\pi$ and $\theta_1 = \pi/N$. Ghost is eliminated and amplitude variations of parent image are eliminated by correction.

correction. At each pixel, the cross-correlation coefficient (r) was calculated between the timeseries (omitting the first 16 images acquired before word presentation) and a 4-s time-delayed box-car reference vector, to create colormaps of activation overlaid on the echo planar images (13).

On each coronal slice, an ROI within the brain (so-called parent ROI) was defined covering the full S/I extent of brain tissue, and 1/3 of the full width of brain tissue in the R/L direction. The ROI over the ghost (so-called ghost ROI) was determined by an $N/2$ shift of the parent ROI. The reduced R/L extent of the parent ROI ensured that the temporal lobe neural activation was not

included (activated pixels would spuriously increase image variance), and that the ghost ROI did not include any part of the brain or surrounding scalp image (such tissue would spuriously decrease the estimate of ghost intensity reduction).

For describing the statistical analysis shown in Table 1, let b_{ptlas} denote an intensity value within a parent or ghost ROI at pixel p , at time t , at slice location l , using algorithm a , for study s . Let P_{ls} , T , L , A , and S denote, respectively, the total number of pixels in the ROIs (defined for each slice location and study), time points, locations, algorithms, and studies. Let $b \cdot$ denote a mean image intensity, where \cdot denotes any combination of p ,

t , l , a , or s to indicate subscripts that were not summed over. Similarly, let σ^2 indicate a mean squared deviation. Means were computed for each of the 128 images in the timeseries, as given by

$$b_{tlas} = \frac{1}{P_{ls}} \sum_p b_{ptlas} \quad [17]$$

and mean squared deviations of these means were computed across repetitions as given by

$$\sigma_{las}^2 = \frac{1}{T-1} \sum_t (b_{tlas} - b_{las})^2 \quad [18]$$

where

$$b_{las} = \frac{1}{T} \sum_t b_{tlas} \quad [19]$$

In Table 1, the first row for each study (or MEAN) gives results using no phase correction, and the second row gives results using image phase correction. The “Mean intensity: parent ROI” entries, denoted b_{as} , are the means over all slice locations of the means of the image intensities across the repetitions, as given by

$$b_{as} = \frac{1}{L} \sum_l b_{las} \quad [20]$$

The “Mean squared deviation: parent ROI” entries, denoted σ_{as}^2 , are computed as the sums across slice locations of the mean squared deviations across repetitions, as given by

$$\sigma_{as}^2 = \frac{1}{L} \sum_l \sigma_{las}^2 \quad [21]$$

These equations apply to ghost ROI columns also. The “Ghost intensity: % of parent image” entries are ratios of b_{as} for ghost ROI divided by b_{as} for parent ROI. For “MEAN” rows, “Mean intensity: parent ROI” and “Mean squared deviation: parent ROI” entries are, respectively, means over the entries for single study dates as given by

$$b_a = \frac{1}{S} \sum_s b_{as} \quad [22]$$

and

$$\sigma_a = \frac{1}{S} \sum_s \sigma_{as}^2 \quad [23]$$

and similarly for the ghost ROI columns.

A nested analysis-of-variance (14, 15) (ANOVA) was performed on the images to confirm that the correction algorithm produced significant intensity changes. The main effects of the nested ANOVA were subject (Levels 1 to 8), slice location (Levels 1 to 16) and correction algorithm (Levels nop and imp). The 128 images (repetitions) in each scan were treated as repeated measurements.

Table 1
Image Phase Correction Evaluation

Study date	Alg	Mean intensity: parent image	Mean squared deviation: parent image	Mean intensity: ghost	Mean squared deviation: ghost	Ghost intensity: % of parent image
25-May	nop	667.8	6.22	85.0	0.31	12.7%
25-May	imp	681.4	6.11	31.1	0.43	4.6%
8-Jun	nop	624.1	2.94	75.0	0.22	12.0%
8-Jun	imp	637.8	2.55	28.5	0.35	4.5%
15-Jun	nop	612.7	5.74	86.2	0.37	14.1%
15-Jun	imp	629.0	4.97	30.5	0.36	4.9%
6-Jul	nop	643.6	3.92	51.1	0.25	7.9%
6-Jul	imp	648.7	3.70	26.7	0.16	4.1%
3-Aug	nop	610.3	5.32	48.6	0.30	8.0%
3-Aug	imp	614.3	5.35	27.7	0.19	4.5%
17-Aug	nop	683.2	7.30	65.3	0.79	9.6%
17-Aug	imp	690.7	7.85	33.6	0.34	4.9%
5-Jan	nop	586.4	2.35	56.7	0.32	9.7%
5-Jan	imp	593.9	2.30	26.3	0.30	4.4%
25-Jan	nop	729.4	2.60	61.4	0.33	8.4%
25-Jan	imp	734.3	2.57	33.3	0.23	4.5%
MEAN	nop	644.7	4.52	66.2	0.36	10.3%
MEAN	imp	653.8	4.40	29.7	0.29	4.5%
F-Ratio		16.5	1.03	2443.1	1.24	6.9*
P(x > F)		<1.0E-6	0.0417	<1.0E-6	<1.0E-6	1.15E-04

Alg: Correction algorithm, nop: none, imp: image phase. * one sided t test for comparison of means assuming unequal variances.

Statistical analysis was performed on parent ROI and ghost ROI intensities separately. The key element of the ANOVA was an F ratio test based on $F = \sigma_{\text{algorithm}}^2 / \sigma_{\text{error}}^2$ comparing the mean squared deviation attributable to the correction algorithm, denoted $\sigma_{\text{algorithm}}^2$, to the mean squared deviation attributable to random error (i.e., unexplained errors), denoted σ_{error}^2 . The numerator $\sigma_{\text{algorithm}}^2$ was computed as the mean squared deviation between image intensities and the mean image intensity over correction algorithms, averaged over subjects and slice locations as given by

$$\sigma_{\text{algorithm}}^2 = \frac{1}{S} \sum_s \left(\frac{1}{L} \sum_l \left(\left(\frac{1}{A-1} \right) \sum_a (b_{las} - b_{ls})^2 \right) \right) \quad [24]$$

The denominator σ_{error}^2 was computed as the mean squared deviation over the repetitions, pooling the squared deviations from nop and imp images as given by

$$\sigma_{\text{error}}^2 = \frac{1}{S} \sum_s \left(\frac{1}{L} \sum_l \left(\frac{1}{A} \sum_a \sigma_{ias}^2 \right) \right) \quad [25]$$

The degrees of freedom (*df*) for this test were (# of subjects) \times (# of slice locations) \times (# of algorithms - 1) (i.e., $df = SL(A - 1)$) for numerator, and (# of subjects) \times (# of slice locations) \times (# of algorithms) \times (# of repetitions) (i.e., $df = SLA(T - 1)$) for denominator. The results of this test are listed under the "Mean intensity" columns in Table 1. To assess the overall benefit and consistency of image phase correction versus no correction, a one-sided *t* test assuming unequal variance was performed across subjects, using the percent ghost intensities listed in the left-most column of Table 1. An F test for unequal variance was performed to confirm that the unequal variance test should be used on this data.

To confirm that ghost correction significantly reduced temporal image intensity variations, an F ratio test was performed to compare the mean squared deviation of image intensities across repetitions for uncorrected images, denoted σ_{nop}^2 , with the same quantity for corrected images, denoted σ_{imp}^2 . These quantities appear in Table 1 under "MEAN" rows and "Mean squared deviation" columns. The F ratio was given by $F = \sigma_{\text{nop}}^2 / \sigma_{\text{imp}}^2$ where

$$\sigma_a^2 = \frac{1}{S} \sum_s \left(\frac{1}{L} \sum_l \sigma_{ias}^2 \right) \quad [26]$$

and *a* is equal to either nop or imp. The degrees of freedom were (# of subjects) \times (# of slice locations) \times (repetitions - 1) (i.e., $SL(T - 1)$) for both numerator and denominator.

Finally, analysis was performed to determine whether the observed increases in parent image signal intensity, and the observed decreases in temporal mean squared deviation, could substantially improve correlation coefficients of activated pixels in fMRI experiments. For each study four coronal slices containing primary auditory cortex (posterior and middle temporal lobe) were selected. Activated pixels were defined as those having *r* values among the top 128, and having $r > 0.323$. The latter constraint corresponded to $P = 0.0001$ (based on *t* test with $df = 126$) and was imposed to ensure that only pixels with strong activation by conven-

tional probability measures were included. When derived using a box-car reference vector, the correlation coefficient can be written

$$r = \sqrt{1 / (1 + (2s_p^2 / \Delta X^2)(2(n - 1) / n))} \quad [27]$$

where ΔX is the difference between the mean image intensity of samples obtained during word presentation versus no-word presentation, s_p^2 is the variance of each mean, and *n* is the number of sample pairs, which is half the number of repetitions (15, p. 126–131, 309–311). Using Eq. [27], the effect of ghost correction over a wide range of *r* values can be estimated, based on observed parent image intensity and standard deviation changes. The activated pixels across all studies had $\Delta X = 10.73$, $r = 0.5178$, and $s_p^2 = 81.82$ ($s_p = 9.045$). The observed s_p^2 serves as an estimate of typical random signal variations present in activated pixels. For each *r*, the corresponding population difference ΔX was derived using Eq. [27] with the observed s_p . The corresponding *r* after ghost correction was then computed by using, for ΔX , the precorrection ΔX multiplied by the observed multiplicative factor increase in parent image intensity (the ratio $b_{\text{imp}} / b_{\text{nop}}$) and, for s_p^2 , the pre-correction s_p^2 multiplied by the observed multiplicative factor decrease in parent image mean squared deviation (the ratio $\sigma_{\text{imp}}^2 / \sigma_{\text{nop}}^2$).

RESULTS

Computer simulation of the correction process using a uniform ellipse of approximate brain slice dimensions is shown in Fig. 1. Constant θ_0 and linear θ_1 phase terms were set to roughly match the ghost seen in an axial brain image, whose analysis is shown in Fig. 2. Details and equation cross-references are provided in the Figure captions. Figure 3 shows, for both simulation and brain image examples, the phase corrections $\theta(x)$ that were applied along *x* at even and odd *k*-space lines. Figure 4 shows, on coronal slices, typical ghost artifact intensity using no phase correction (nop), image phase correction (imp), and calibration scan correction (cal). Column I shows a relatively common situation in which ghost intensity is reduced using either correction, but is reduced more with image phase correction. Column II shows the relatively uncommon situation where the intensity of the ghost is reduced with image phase correction, but is made worse by calibration scan correction. Figure 5a shows the raw data from the calibration scans used in Fig. 4, and Fig. 5b shows the phase corrections derived from this raw data. The calibration scan raw data for Image I had a narrow range of temporal offsets (peaks were -1.0 ± 0.5 data point from center along k_x), while that for Image II had a wide range of temporal offsets (peaks were -3 to 5 data points from center). Separately for even and odd *k*-space lines, calibration scan correction extracts the temporal offset of the *k*-space line having the maximum amplitude data point (usually the first two *k*-space lines), and applies that offset to all lines. For Image I, phase corrections derived from the calibration scan provided a good linear approximation of the image phase correction for Image I, and the ghost intensity decreased with calibration scan correction. For Image II, linear phase corrections derived from the calibration

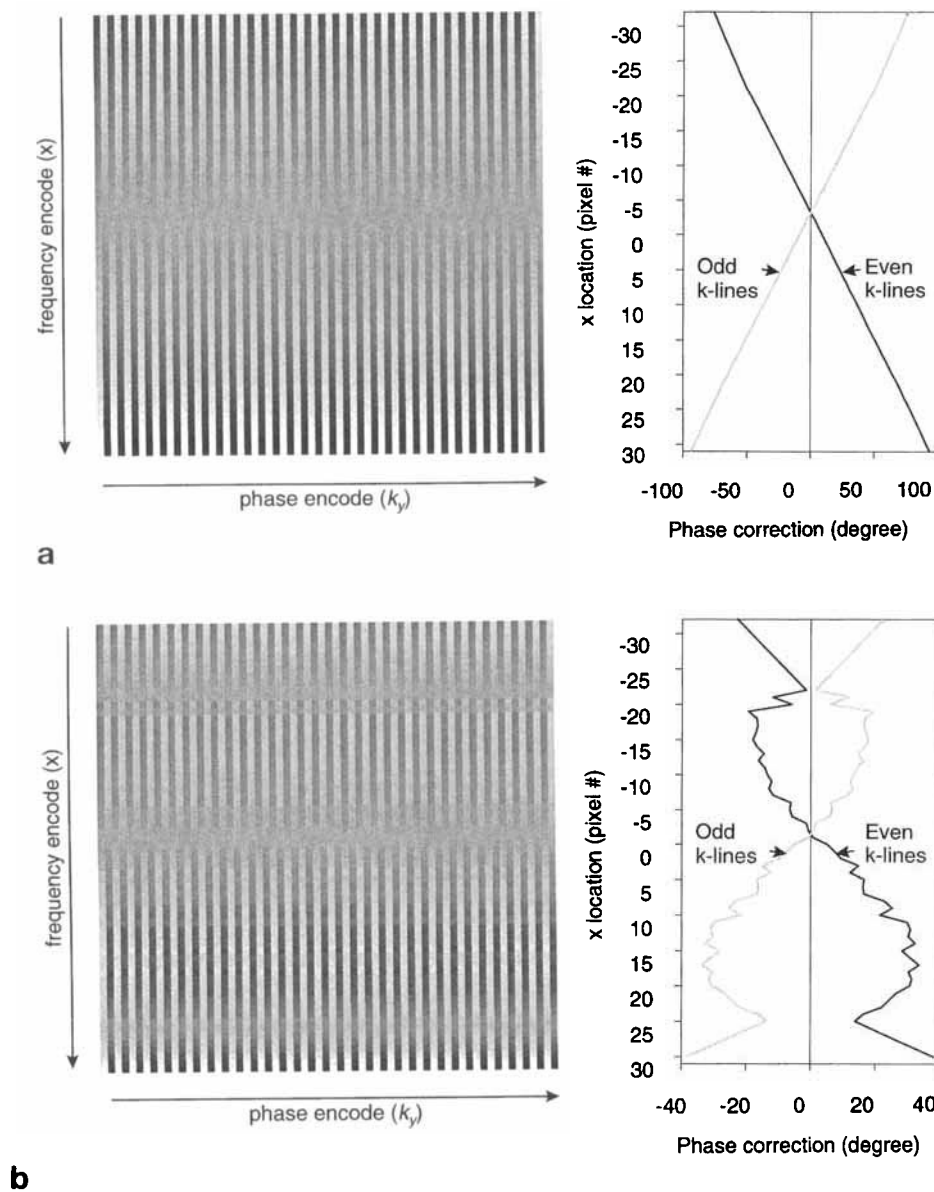


FIG. 3. Subtraction of phase images in (x, k_y) domain from Figs. 1 and 2 (displayed in g1 and g2 in each figure). (a) g1 minus g2 from Fig. 1 reveals the spatial distribution of image phase corrections that were applied to the original data in the (x, k_y) domain. Linear dependence of the correction in the x direction was found. Graph shows phase corrections for even k -lines (black line) and odd k -lines (gray line). (b) Same as (a), using axial head scan data shown in Fig. 2. Correction deviates significantly from linear in the periphery of the image along the frequency encode (x) direction.

scan approximated image phase corrections very poorly, and the ghost intensity increased.

Table 1 shows that the image intensity within the ghost ROI was reduced from 66.2 ± 14.5 (range: 48.6–86.2) to 29.7 ± 2.8 (range: 26.3–33.3), corresponding to a percent reduction in the ghost intensity of $54\% \pm 9\%$ (range: 43–65%). This reduction was highly significant by F ratio test ($P < 1.0E-6$). Before correction, ghost intensity was $10.3\% \pm 2.1\%$ (range: 7.9–14.1%) of parent image intensity, while after correction it was $4.5\% \pm 0.2\%$ (range: 4.1–4.9%). Referring to the trigonometric interpretation, Eq. [10], the average θ before correction was 5.87° (range: 4.54° – 8.00°) while the average θ was 2.60° (range: 2.36° – 2.78°) after correction. Across subjects, the

average intensity within parent ROI increased slightly (644.7 ± 4.5 to 653.8 ± 4.4), but because the pooled mean squared deviation of the image intensities across repetitions was small (average of 4.40 and 4.52), this increase was highly significant by F ratio test ($P > 1.0E-6$). The sum of the squares of ghost and parent image intensity was nearly constant, independent of whether the correction was applied. Referring to the left-most column, image phase correction significantly reduced residual ghost intensity ($t = 6.90$, $df = 7$, $P = 1.15E-4$) and variation ($F = 98.9$, $df = 7$, $P = 1.97E-6$), as measured across subjects, meaning that initial ghosts were similar and ghost correction improvements were consistently obtained in each and every subject. Table 1 also shows that variations in image intensity across repetitions were significantly less after correction within both parent and ghost ROI. Specifically, reduction in mean squared deviation (σ_a^2) within the parent ROI was $4.52 - 4.40 = 0.12$ ($P = 0.042$ by F ratio test), while the reduction in mean squared deviation within the ghost ROI was $0.36 - 0.29 = 0.07$ ($P < 1.0E-6$ by F ratio test).

Analysis using Eq. [27] revealed that ghost correction will generally increase r values of activated pixels in functional MRI. Based on the observed decrease in temporal mean squared deviation of 2.79% (from 4.52 to 4.40), and observed increase in parent image intensity of 1.41% (from 644.7 to 653.8), expected improvement in r was computed to be 2.0% at $r = 0.5$ (i.e., $r = 0.50$ before correcting to $r = 0.510$ after correction), and monotonically decreasing from 2.7% to 0.5% as r varied from 0.1 to 0.9. Consistent with this, ghost correction improved r values of activated pixels in the eight subjects. Across the eight subjects, in the activated pixels the mean r value increased $0.85 \pm 0.89\%$ (range: -0.07% to 2.74%), and the increase in the number of pixels exceeding the precorrection threshold (starting from 128) ranged from zero to six. Figure 6 shows activation maps from two typical slices in two fMRI auditory studies. In the May 25 study, image phase correction provided 0.69% increase in the mean correlation coef-

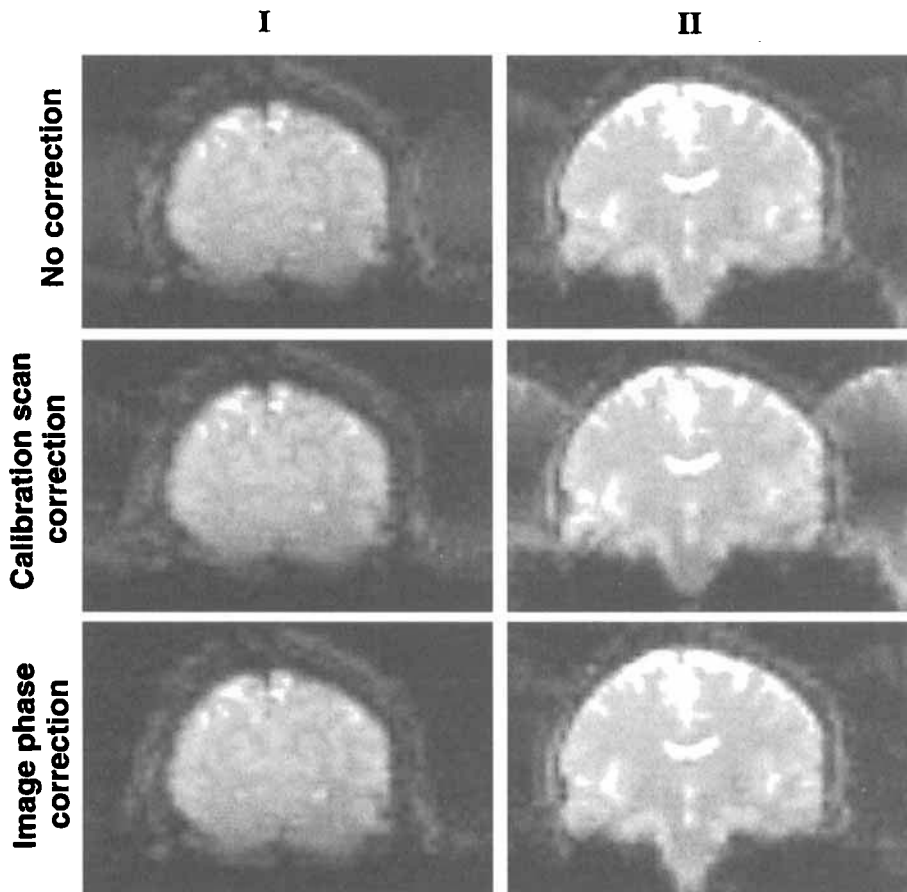


FIG. 4. Coronal images showing typical $N/2$ ghost artifacts using no phase correction (nop), calibration scan correction (cal), and image phase correction (imp). Column I shows a common situation where the intensity of the ghost artifact is in the order $\text{nop} > \text{cal} > \text{imp}$. Ghosts are 11.3%, 8.2%, and 3.5% of the parent image intensity. It is common for the periphery of the image along the frequency direction to show less improvement than the central region. Column II shows the relatively uncommon situation (approximately 1–2 per 16 slices) where the intensity of the ghost artifact is in the order $\text{cal} > \text{nop} > \text{imp}$. Ghosts are 11.0%, 38.8%, and 6.8% of the parent image intensity. In II, calibration scan correction worsens the ghost artifact as a result of poor estimation of the actual phase offsets occurring during image acquisition. (W/L: 1300/650 for all images, set to highlight ghost artifact).

ficient of the activated pixels ($\bar{r} = 0.433$ before correction, $\bar{r} = 0.436$ after correction), but no increase in the number of pixels exceeding the threshold (72 pixels with $r > 0.323$ in each). In the June 8 study, image phase correction provided 1.58% increase in the mean r of the activated pixels ($\bar{r} = 0.507$ before correction, $\bar{r} = 0.515$ after correction), and four additional pixels (from 128 to 132) exceeded the pre-correction r threshold. These changes are not significant ($P = 0.22$ for one-sided t test using pooled data) but are consistent with the estimates based on ghost intensity changes.

DISCUSSION

In eight subjects, image phase correction consistently reduced residual ghost intensity. Phase correction based on calibration scan also reduced the ghost artifact and was a viable approach to the ghosting problem. However, our calibration scan algorithm (described in the Introduction), did not work as well as image phase correction, and significantly increase ghost intensity in approximately

10% of images (that is, in all images at about 1–2 of 16 slice locations). Increases in ghost intensity were the result of large differences between the phase estimates derived from the calibration scan and the phase offsets that occurred during image acquisition. These increases were most pronounced in the periphery of the image along the frequency encode direction. They reflect the fact that phase errors deviated substantially from linear in x , and the fact that signal intensity is relatively low in the periphery (due to lower RF coil sensitivity, larger gradient nonlinearity, and larger main field distortions) so that central spins rather than peripheral spins contribute most to the echo signal and largely determined the echo offset.

The corrected images presented in this paper were derived using $\theta = \theta(x)$, where phase errors were averaged over y at each x . The fact that the differences between the phases of $\hat{M}_{\text{even}}(x,y)$ and $\hat{M}_{\text{odd}}(x,y)$ were largely independent of y indicates that $\theta(x)$ contains nearly the same information as $\theta(x,y)$, and ghost correction based on $\theta(x,y)$ would not be substantially different from that based on $\theta(x)$. When using $\theta = \theta(x)$, the FOV needs to be somewhat greater than

the object size. Overlap of ghost and parent image is permitted provided there is at least one pixel (which will lie at the center along the phase encode direction) that has no overlap. The phase error of this pixel would then represent the phase error for the entire row. It is advised to have five to ten nonoverlapping pixels in the center to allow averaging. Pixels with flow within the sagittal sinus should be avoided, and correction for those rows can be estimated by interpolation. Pixels containing both parent and ghost image might be used to determine the phase correction but analysis would be much more complex. In such an algorithm, one would be comparing pixels separated by $1/2$ the FOV and therefore it would be necessary to take into account phase variations across the image from other sources. These variations can be determined only with additional reference data (16–18). Correction of the entire image using $\theta(x,y)$ demands a FOV twice the object size, doubling data acquisition time for a given pixel size. It might be more reliable to simply discard the odd or even k -space lines of data with a FOV

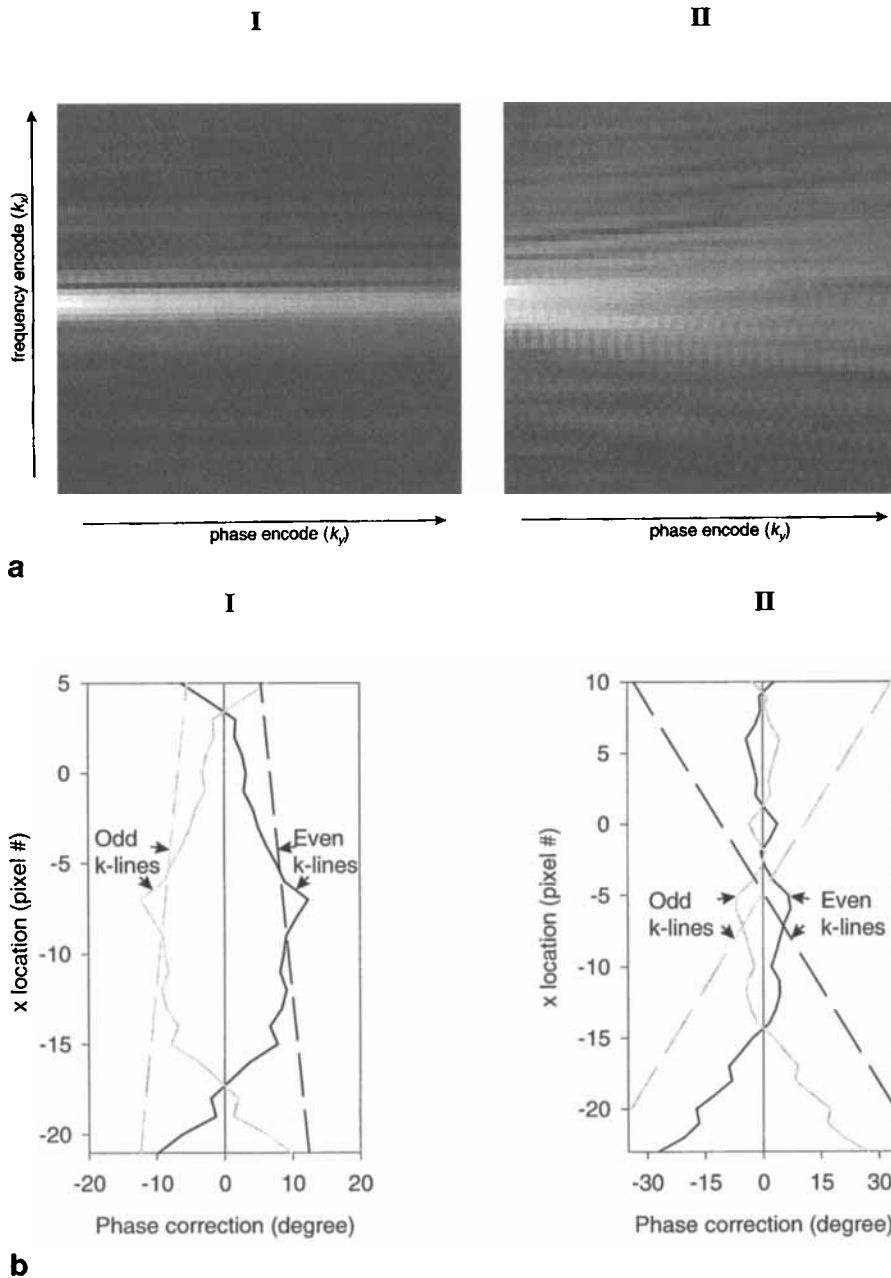


FIG. 5. Evaluation of calibration scan results in Fig. 4, columns I and II. (a) Amplitude of calibration scan raw data (displayed in (k_x, k_y) domain after time reversal of odd lines). (b) Plots of both image phase corrections (solid lines) and linear calibration scan phase corrections (dashed lines) for even (black) and odd (gray) k -space lines. Because phase encode (k_y) is turned off, vertical lines or raw data should have peak at or near $k_x = 0$ (horizontal center of image), and, except for T_2 decay, should not vary as a function of k_y . Temporal offsets as a function of x in the (x, k_y) domain. In I, successive echos of the calibration scan were well aligned, and the plots show that the resulting phase corrections were appropriate for all k lines. In II, successive echos were poorly aligned in the calibration scan (peak location varied from -3 to 5 along k_x), and the plots show that the resulting phase corrections were too large, producing a higher intensity ghost. In both examples, the calibration scan correction at the periphery in the frequency encode (x) direction differed most from the image phase correction. The ghost intensity was correspondingly higher in these regions.

equal to the object size to eliminate phase problems in the data set, or apply schemes based on specific k -space oversampling trajectories (19–21). A method to remove EPI ghosting from so-called parametric phase distortions,

having similar formalism to that used for image phase correction presented here, has been recently described to correct constant and linear phase corrections (22).

When $\theta = \theta(x)$, image phase correction can be written in the formalism presented previously by Bruder *et al.* (3, page 320–321). Relating Eq. [8] above to Eqs. [23] and [24] of ref. 3, the filter $\tilde{F}(x)$ in Eq. [27] of ref. 3 reduces to $\exp(-2i\theta(x))$, and Eq. [25] for the corrected image is given by $M_{\text{odd}}(x, y) + M_{\text{even}}(x, y)\exp(-2i\theta(x))$, which is equal to our Eq. [12] for the corrected image times a phase factor $\exp(+i\theta(x))$ which has no effect on the magnitude image. However, in order for Eq. [27] in ref. 3 to match our algorithm, averaging over y must be performed at all lines having ghost intensity in the ghost-only region. This requirement is suggested by the statement given below Eq. [27], but it is important to add that the averaging should not include pixels in the overlap region. Also, the filter $\tilde{F}(x)$ given by Eq. [27] would be affected by amplitude differences between the images reconstructed with only even and odd k -space lines. The effects of amplitude differences on filter performance are not known, but such effects are explicitly avoided in image phase correction. They are presumably harmful, because such amplitude differences cannot be traced back mathematically to phase distortions caused by gradient actions defined uniquely on even versus odd k -space lines.

Image phase correction using θ cannot correct for the $N/2$ ghost contribution arising from main field distortion. When there is mainfield distortion, the integrands of Eq. [1] and [2] require additional multiplicative factors given by

$$\exp(i\gamma\Delta B t)\exp(-i\gamma m\Delta B t_1)\exp(i\gamma\Delta B T E) \quad [28]$$

where $\Delta B \equiv \Delta B(x, y)$ is the main field distortion, m indexes the phase encode step, t_1 is the interval between

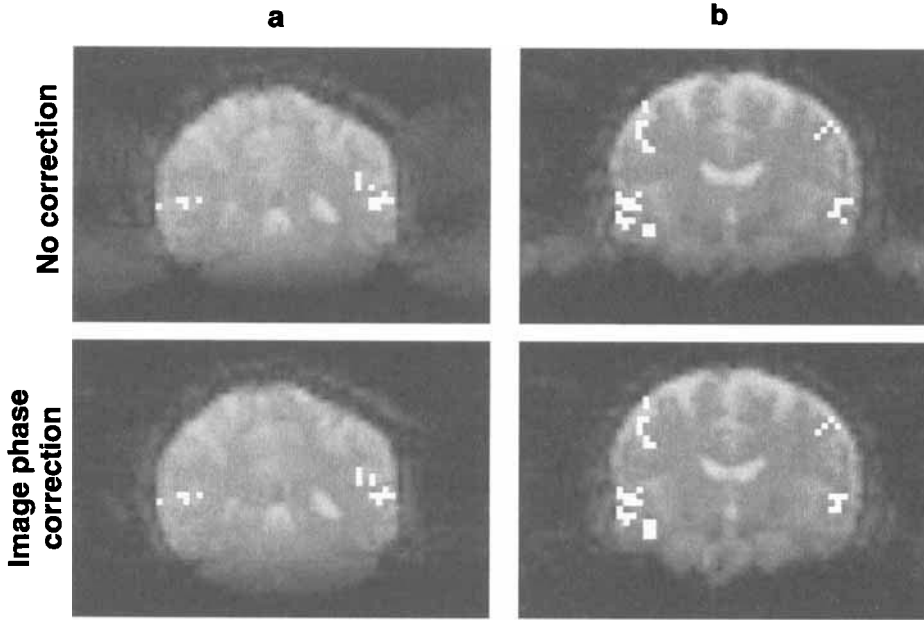


FIG. 6. Comparison of activation maps from primary auditory cortex (superior and middle temporal lobes bilaterally) derived with no correction versus image phase correction reveal only slight differences. In May 25 and June 8 study, activated pixels were those having r values among the highest 72 and 128, respectively, are colored white. For each study, one representative image is shown. (a) May 25: image phase correction resulted overall in a 0.69% increase in r values of activated pixels, but had no increase in the number of pixels above the r threshold of 0.323. (b) June 8: phase correction resulted overall in a 1.58% increase in r values, and four additional (128 to 132, two additional shown in this figure) above the pre-correction $r = 0.362$ threshold.

successive y blip gradients and TE is the echo time (defined as the time when data point $(k_x, k_y) = 0$ is acquired in each TR). Defining $\beta_x(x, y) = \Delta B(x, y)/G_x \Delta x$ and $\beta_y(x, y) = \frac{1}{2} \Delta B(x, y)/G_x \Delta x$, ($\Delta x =$ pixel spacing) the reconstructed image is written

$$\hat{M}(x, y) = \frac{1}{2} \exp(i\gamma \Delta B TE)$$

$$\cdot \left[\left(M(x + \beta_x(x, y), y - \beta_y(x, y)) + M\left(x + \beta_x(x, y), y - \beta_y\left(x, y - \frac{N}{2}\right) - \frac{N}{2}\right) \right) \exp(i\theta(x, y)) + (M(x - \beta_x(x, y), y - \beta_y(x, y)) - M\left(x - \beta_x(x, y), y - \beta_y\left(x, y - \frac{N}{2}\right) - \frac{N}{2}\right)) \exp(-i\theta(x, y)) \right] \quad [29]$$

Main field distortion causes the images from even and odd k -space lines (the first and second terms, respectively) to have unequal magnitude but does not cause them to have differences in phase. This is best seen by first order expansion of Eq. [29] with respect to θ , β_x , and β_y . After simplification and separation of the terms contributing to the ghost, Eq. [29] is given by

$$\hat{M}(x, y) \cong \text{parent image terms} + \exp(i\gamma \Delta B TE) \cdot \left(\beta_x\left(x, y - \frac{N}{2}\right) \frac{dM\left(x, y - \frac{N}{2}\right)}{dx} + iM\left(x, y - \frac{N}{2}\right)\theta(x, y) \right) \quad [30]$$

The second term within the parentheses in the θ contribution that is imaginary clearly does not reduce amplitude distortion given by the first term. Since the difference in amplitude between $\hat{M}_{\text{even}}(x, y)$ and $\hat{M}_{\text{odd}}(x, y)$ depends on the undistorted image M as well as offsets β , both initially unknown, the unique solution must be found iteratively. An algorithm that addresses this problem with the aid of an additional EPI chemical shift image has recently been reported (23).

It is interesting to consider whether this analysis shows that the ghost intensity can simply be added back to the parent image based on some appropriate $\theta(x, y)$. Using this scenario, $\theta(x, y)$ would not be computed from even and odd echo images, but rather would be determined solely by what was necessary to entirely remove the ghost, as in Eq. [11]. The corrected image would be equal to the square root of the sum of the squares of the parent image and the ghost image. Analysis shows that trigonometric addition of intensities is theoretically correct provided there are no other sources of phase encode artifact. Unfortunately, such an approach is not legitimate because the ghost contributions from main field distortions do not follow the trigonometric distribution.

REFERENCES

1. F. Farzaneh, S. J. Riederer, N. Pelc, Analysis of T2 limitations and off-resonance effects on spatial resolution and artifacts in echo-planar imaging. *Magn. Reson. Med.* **14**, 123-139 (1990).
2. D. A. Feinberg, R. Turner, P.E. Jakab, M. von Kienlin, Echo-planar imaging with asymmetric gradient modulation and inner-volume excitation. *Magn. Reson. Med.* **13**, 162-169 (1990).
3. H. Bruder, H. Fischer, H. E. Reinfelder, F. Schmitt, Image reconstruction for echo planar imaging with nonequidistant k -space sampling. *Magn. Reson. Med.* **23**, 311-323 (1992).
4. C. Boesch, R. Gruetter, E. Martin, Temporal and spatial analysis of fields generated by eddy currents in superconducting magnets: optimization of corrections and quantitative characterization of magnet/gradient systems. *Magn. Reson. Med.* **20**, 268-284 (1991).
5. D. A. Feinberg, K. Oshio, Phase errors in multi-shot echo planar imaging. *Magn. Reson. Med.* **32**, 535-539 (1994).
6. K. Butts, S. J. Riederer, R. L. Ehman, R. M. Thompson, C. R. Jack.

- Interleaved echo planar imaging on a standard MRI system. *Magn. Reson. Med.* **31**, 67–72 (1994).
7. K. F. King, C. R. Crawford, J. K. Maier, Correction for filter-induced ghosts in echo planar imaging, in "Proc., SMR, 3rd Annual Meeting, Nice, France, 1995," p. 105.
 8. E. C. Wong, Shim insensitive phase correction for EPI using a two echo reference scan, in "Proc., SMRM, 11th Annual Meeting, Berlin, Germany, 1992," p. 4514.
 9. A. Jesmanowicz, E. C. Wong, J. S. Hyde, Phase correction for EPI using internal reference lines, in "Proc., SMRM, 12th Annual Meeting, New York, 1993," p. 1239.
 10. J. K. Maier, M. Vevrek, G. H. Glover, Correction of NMR data acquired by an echo planar technique. US Patent #5,151,656 (1992).
 11. M. H. Buonocore, R. J. Maddock, L. Gao, T. E. Nordahl, Cortical activation response to the semantic and emotional components of words. *Radiology* **193(P)**, 136 (1994).
 12. J. Talairach, P. Tournoux, "Co-Planar Stereotaxic Atlas of the Human Brain. 3-Dimensional Proportional System: An Approach to Cerebral Imaging," Thieme Medical Publishers, Inc., New York, 1988.
 13. P. A. Bandettini, A. Jesmanowicz, E. C. Wong, J. S. Hyde, Processing strategies for time-course data sets in functional MRI of the human brain. *Magn. Reson. Med.* **30**, 161–173 (1993).
 14. R. R. Sokel, F. J. Rohlf, "Biometry," 2nd ed., pp. 278–281, W.H. Freeman, New York, 1981.
 15. J. H. Zar, "Biostatistical Analysis," 2nd ed., pp. 258–259, Prentice-Hall, Englewood Cliffs, NJ, 1984.
 16. X. Wan, G. T. Gullberg, D. L. Parker, Reduction of geometric distortion in echo-planar imaging using a multi-reference scan, in "Proc., SMR, 3rd Annual Meeting, Nice, France, 1995," p. 103.
 17. A. Jesmanowicz, E. C. Wong, J. S. Hyde, Self-correcting EPI reconstruction algorithm, in "Proc., SMR, 3rd Annual Meeting, Nice, France, 1995," p. 619.
 18. J. B. Mandeville, R. M. Weisskoff, L. Garrido, Reduction of eddy-current induced Nyquist ghosts and sampling artifact, in "Proc., SMR, 3rd Annual Meeting, Nice, France, 1995," p. 613.
 19. S. Posse, G. Tedeschi, R. Risinger, R. Ogg, D. Le Bihan, High speed 1H spectroscopic imaging in human brain by echo planar spatial-spectral encoding. *Magn. Reson. Med.* **33**, 34–40 (1995).
 20. Q. X. Yang, S. Posse, D. Le Bihan, M. B. Smith, Over-sampled echo-planar imaging, in "Proc., SMR, 3rd Annual Meeting, Nice, France, 1995," p. 615.
 21. S. Hirata, Y. Bito, E. Yamamoto, Signal-to-noise ratio improvement using multiple echo-trains in high speed 4D MRSI based on the echo planar technique in "Proc., SMR, 3rd Annual Meeting, Nice, France, 1995," p. 1903.
 22. J. W. Goldfarb, F. Schmitt, H. Fischer, E. M. Haacke, J. L. Duerk, A method to remove ghosting from parametric phase distortions in EPI in "Proc., SMR, 3rd Annual Meeting, Nice, France, 1995," p. 759.
 23. D. C. Alsop, Correction of ghost artifacts and distortion in echo-planar MR imaging with an iterative image reconstruction technique, *Radiology* **197(P)**, 388 (1995).
 24. M. H. Buonocore, R. J. Perlmutter, G. Kirk, L. A. Shepp, A new analytic simulation method for magnetic resonance (MR) imaging, in "Proc., SMRM, 4th Annual Meeting, London, 1985," p. 576.